Electronic Supplementary Material (ESI) for Journal of Materials Chemistry A.

Supporting Information

Highly Efficient Flexible Li-S Full Batteries with Hollow Ru-RuO$_{2-x}$ Nanofibers as Robust Polysulfide Anchoring-catalysts and Lithium Dendrite Inhibitors

Yuan Tian,[a] Ming Yang,*[b] Cheng Wang *[a]

Dr. Y. Tian, Prof. C. Wang

Institute for New Energy Materials and Low-Carbon Technologies, School of Materials Science and Engineering, Tianjin Key Laboratory of Advanced Functional Porous Materials, Tianjin University of Technology, Tianjin 300384, China. E-mail: cwang@tjut.edu.cn

Prof. M. Yang

National Key Laboratory of Science and Technology on Power Sources, Tianjin Institute of Power Sources, Tianjin 300384, China. E-mail: yangmingnk@163.com

Contents:

Li/RuO_2@PAN symmetric cells at 1 mA cm^{-2} and 1 mAh cm^{-2}.

Fig. S14. Detailed voltage profiles of Li and Li/Ru-RuO_{2-x}@NC symmetric cells at 1 mA cm^{-2} and 1 mAh cm^{-2}.

Fig. S15. SEM image of Li/Ru-RuO_{2-x}@NC electrode over cycling 200h at 1 mA cm^{-2} and 1 mAh cm^{-2}.

Fig. S16. EIS plots of bare Li and Li/Ru-RuO_{2-x}@NC symmetric cells over cycling 200h.

Fig. S17. (a) Schematic diagram for the S/Ru-RuO_{2-x}@NC cathode and the Li/Ru-RuO_{2-x}@NC anode; (b) Schematic configuration of the S/Ru-RuO_{2-x}@NC||Li/Ru-RuO_{2-x}@NC full battery and a traditional Li-S battery.

Fig. S18. Voltage profiles of (a) S/RuO_{2-x}@NC||Li/RuO_{2-x}@NC, (b) S/Ru@NC||Li/Ru@NC and (c) S/RuO_2@PAN||Li/RuO_2@PAN cells at different current rates.

Fig. S19. Magnified XRD patterns of RuO_2@PAN, RuO_{2-x}@NC and Ru-RuO_{2-x}@NC.

Fig. S20. (a) Ru-3d and (b) total DOS patterns of RuO_2, RuO_{2-x}, Ru-RuO_{2-x} and Ru.

Fig. S21. Geometrically stable configurations of RuO_2, RuO_{2-x}, Ru-RuO_{2-x} and Ru.

Fig. S22. (a) The optimized molecular structures of the most stable isolated LiPSs in the ground state and (b) the shortest distances of Li-S and S-S bonds.

Fig. S23. DFT calculation results of optimized geometrical configurations of various LiPSs on (a) RuO_2, (b) RuO_{2-x}, (c) Ru-RuO_{2-x} and (d) Ru.

Fig. S24. (a) Energy barrier of Li_2S decomposition and (b) Li^+ diffusion energy barrier on RuO_2, RuO_{2-x}, Ru-RuO_{2-x} and Ru.

Fig. S25. Binding energy and optimized geometrical configurations of a Li atom with Ru-RuO_{2-x}, RuO_{2-x}, RuO_2 and Ru.

Table S1. BET results summary of RuO_2@PAN, RuO_{2-x}@NC, Ru-RuO_{2-x}@NC and Ru@NC composites according to nitrogen adsorption-desorption isotherm.

Characteristics	RuO_2@PAN	RuO_{2-x}@NC	Ru-RuO_{2-x}@NC	Ru@NC
SSA ($m^2\ g^{-1}$)	28.65	81.75	344.19	196.81
Pore volume ($m^3\ g^{-1}$)	0.05	0.15	0.55	0.51
Pore width (nm)	5.88	3.78	5.08	3.77

Table S2. Electrochemical performance comparison of this work with that of other Ru-based composite cathodes in recent works.

Cathode material	**Sulfur loading (mg cm^{-2})**	**Initial capacity (mAh g^{-1})**	**Capacity fading rate & cycles**	**Rate capability (mAh g^{-1})**	**Ref.**
S/Ru-RuO_{2-x}@NC	**1.4**	**1.0 C, 1095**	**0.015%, 1000**	**8.0 C, 835**	**This work**
RuO_2@NMCs/S	1.5	0.5 C, 1065	0.07%, 500	5.0 C, 634	[1]
Graphene/RuO_2/S	1.5	1.0 C, 685	0.054%, 800	2.0 C, 543	[2]
S/RuO_2	1.4	1.0 C, 833	0.08%, 500	5.0 C, 479	[3]
RuO_2-UPCS@S	2.0	0.2 C, 1301	--,--	2.0 C, 985	[4]
3D CNTs@10% RuO_2@Li_2S_6	2.0	0.5 C, 1060	0.06%, 1000	2.0 C, 750	[5]

Table S3. The relevant parameters of the active materials in the Ru-based cathodes.

Volume of 1.0M Li_2S_6 catholyte (μL)	**Sulfur mass (mg)**	**Sulfur loading (mg cm^{-2})**	**Electrolyte/S ratio (E/S, μL mg^{-1})**
10	1.9	1.7	15.8
24	4.6	4.1	9.6
32	6.1	5.4	8.5
40	7.7	6.8	7.8

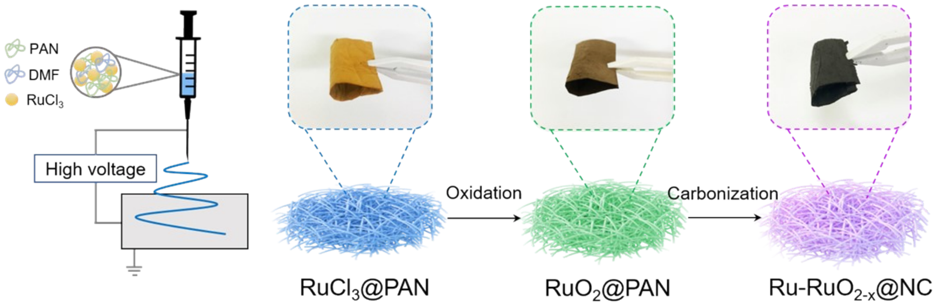

Fig. S1. Schematic illustration of the synthetic procedure for the Ru-based products and the corresponding digital photos.

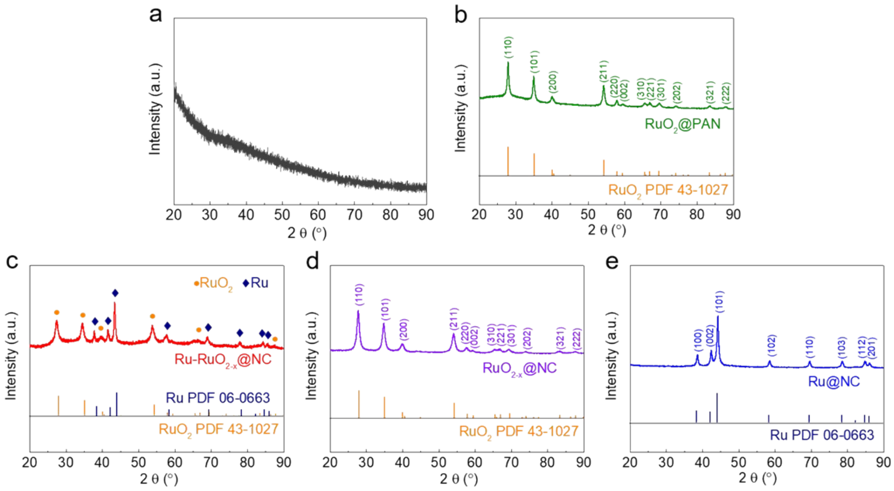

Fig. S2. XRD patterns of (a) $RuCl_3$@PAN-O, (b) RuO_2@PAN, (c) Ru-RuO_{2-x}@NC, (d) RuO_{2-x}@NC and (e) Ru@NC.

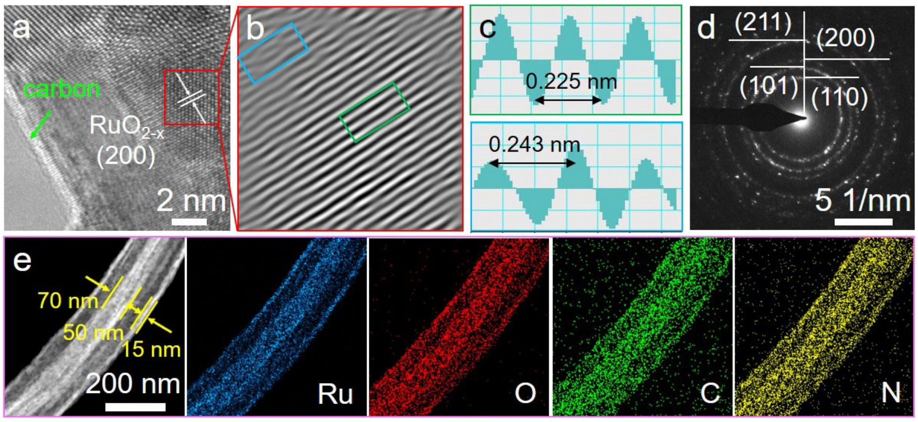

Fig. S3. (a) HRTEM image, (b) IFFT lattice image, (c) lattice spacing profiles at the selected areas in green and blue, (d) SAED pattern at the selected area in red and (e) high-magnification elemental mappings of RuO_{2-x}@NC.

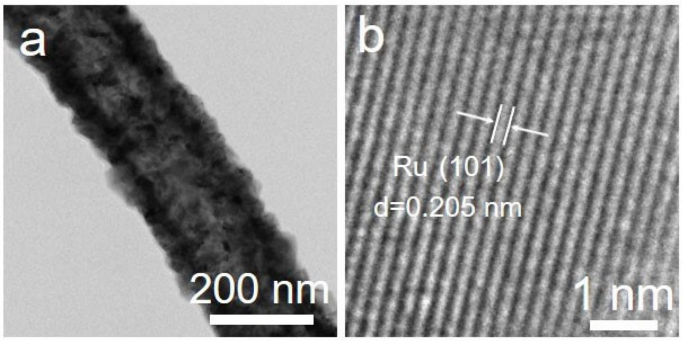

Fig. S4. (a) TEM image and (b) HRTEM image of Ru@NC.

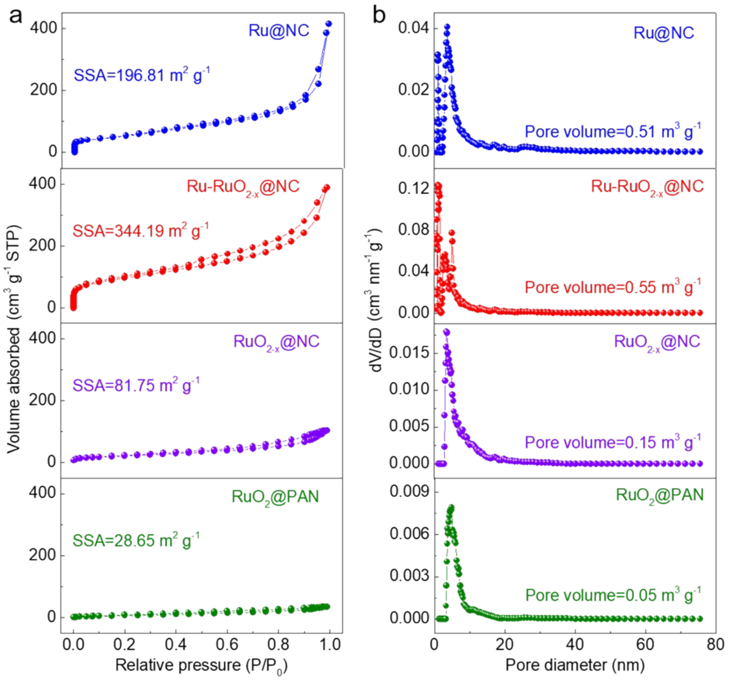

Fig. S5. (a) N_2 adsorption/desorption isotherms and (b) pore size distributions of RuO_2@PAN, RuO_{2-x}@NC, Ru-RuO_{2-x}@NC and Ru@NC.

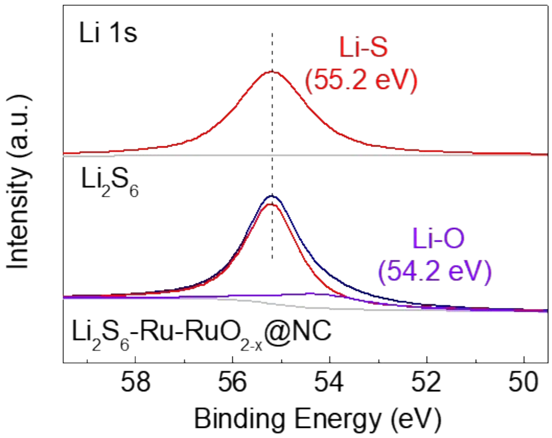

Fig. S6. Li 1s high-resolution XPS spectra of Li_2S_6 and Li_2S_6-Ru-RuO_{2-x}.

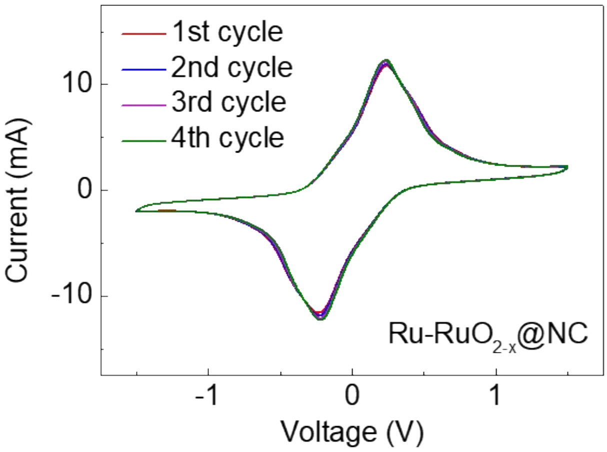

Fig. S7. CV curves of a Ru-Ru_{2-x}@NC symmetric cell for several cycles.

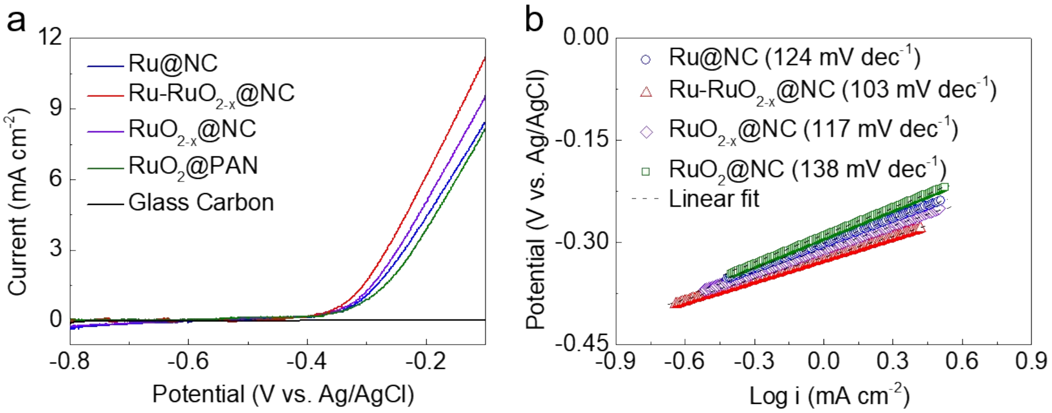

Fig. S8. (a) LSV curves of Li_2S oxidization and (b) Tafel plots of Li_2S oxidization on RuO_2@PAN, RuO_{2-x}@NC, Ru-RuO_{2-x}@NC and Ru@NC.

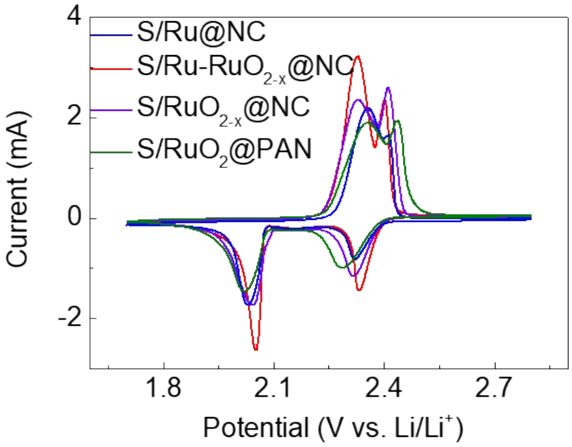

Fig. S9. CV curves of different Li-S batteries for S/Ru-RuO_{2-x}@NC, S/RuO_{2-x}@NC, S/Ru@NC and S/RuO_2@PAN cathodes.

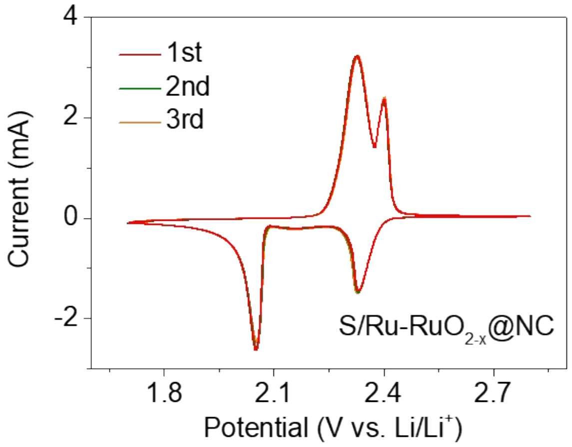

Fig. S10. CV curves of the Li-S battery for the S/Ru-RuO$_{2-x}$@NC cathode with a scanning rate of 0.1 mV s^{-1}.

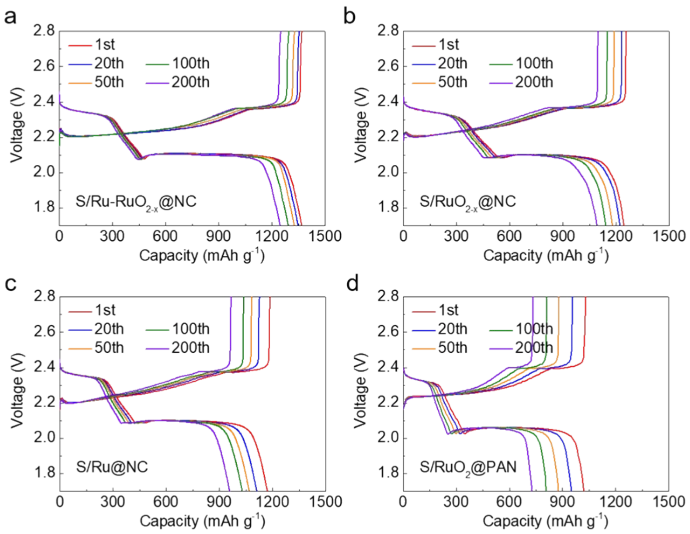

Fig. S11. Charge-discharge profiles of the Li-S batteries for (a) the S/Ru-RuO$_{2-x}$@NC cathode, (b) the S/RuO$_{2-x}$@NC cathode, (c) the S/Ru@NC cathode and (d) the S/RuO$_2$@PAN cathode.

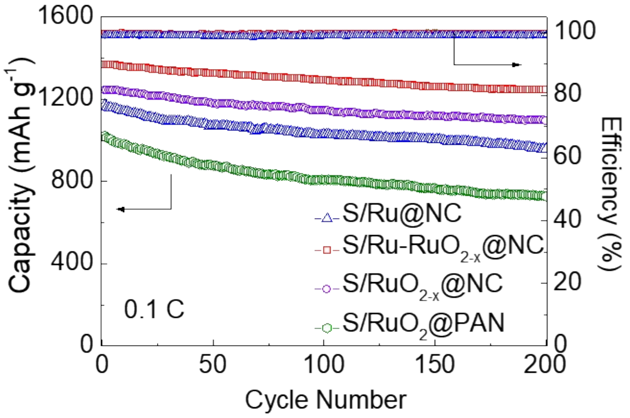

Fig. S12. Cycling performances at 0.1 C of the Li-S batteries for the S/Ru-RuO$_{2-x}$@NC, S/RuO$_{2-x}$@NC, S/Ru@NC and S/RuO$_2$@PAN cathodes.

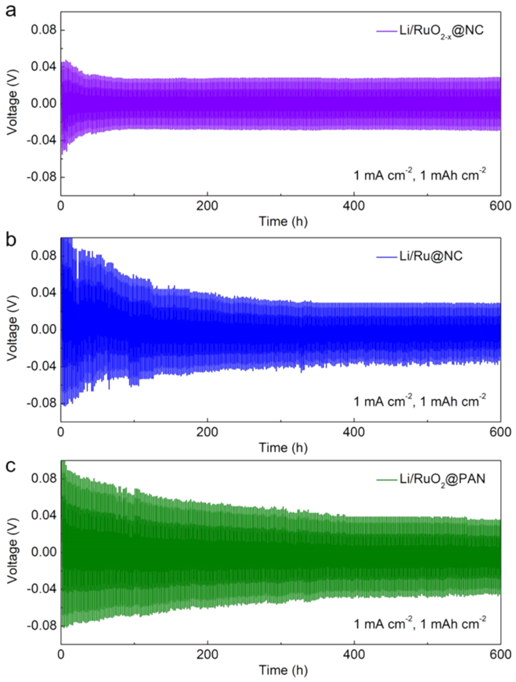

Fig. S13. Cycling performance for (a) Li/RuO_{2-x}@NC, (b) Li/Ru@NC and (c) Li/RuO_2@PAN symmetric cells at 1 mA cm^{-2} and 1 mAh cm^{-2}.

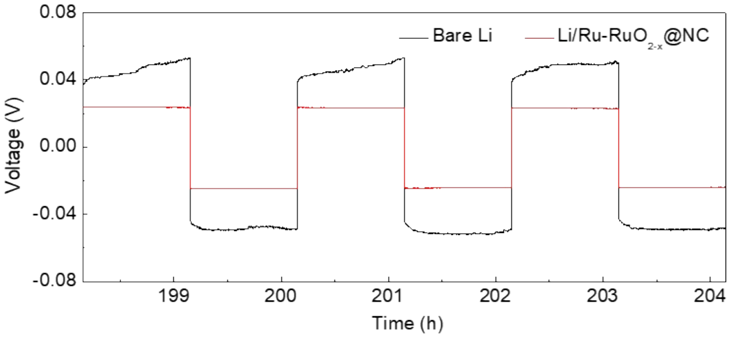

Fig. S14. Detailed voltage profiles of Li and Li/Ru-RuO_{2-x}@NC symmetric cells at 1 mA cm^{-2} and 1 mAh cm^{-2}.

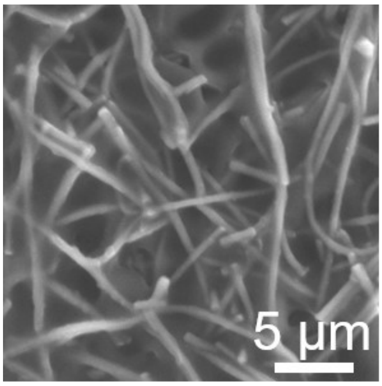

Fig. S15. SEM image of Li/Ru-RuO_{2-x}@NC electrode over cycling 200h at 1 mA cm^{-2} and 1 mAh cm^{-2}.

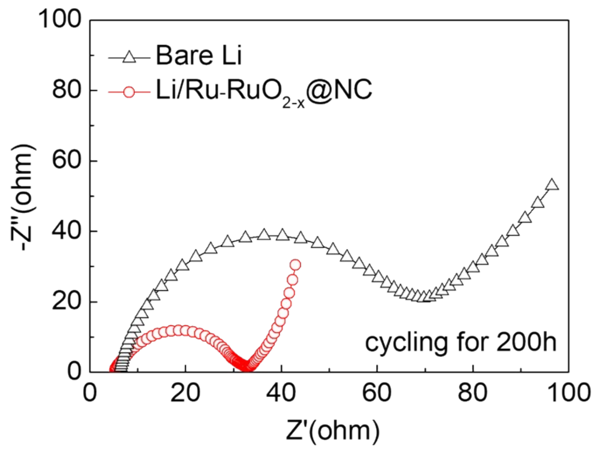

Fig. S16. EIS plots of bare Li and Li/Ru-RuO_{2-x}@NC symmetric cells over cycling 200h.

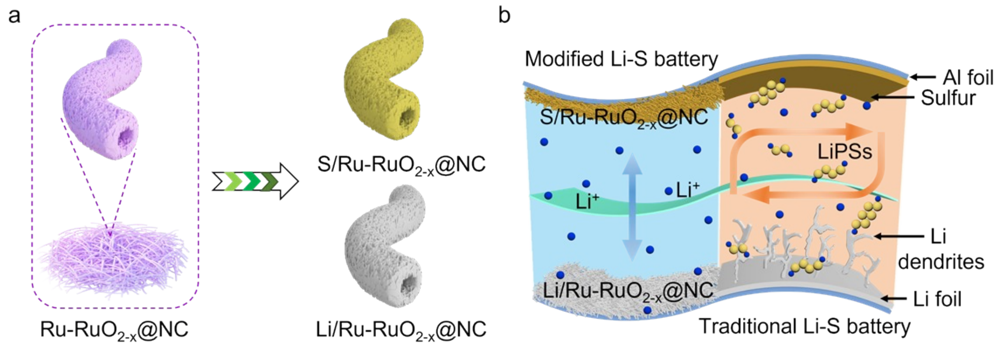

Fig. S17. (a) Schematic diagram for the S/Ru-RuO_{2-x}@NC cathode and the Li/Ru-RuO_{2-x}@NC anode; (b) Schematic configuration of the S/Ru-RuO_{2-x}@NC||Li/Ru-RuO_{2-x}@NC full battery and a traditional Li-S battery.

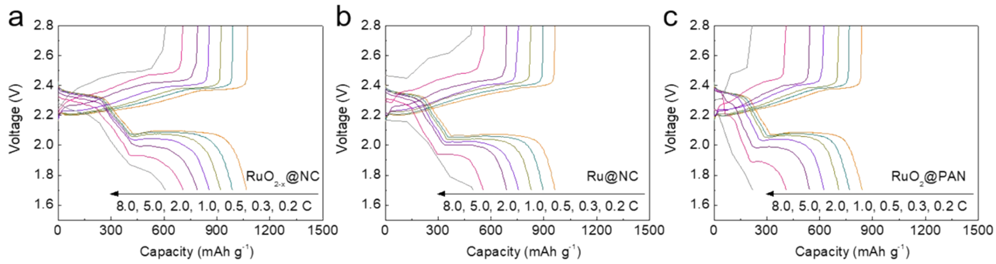

Fig. S18. Voltage profiles of (a) S/RuO_{2-x}@NC||Li/RuO_{2-x}@NC, (b) S/Ru@NC||Li/Ru@NC and (c) S/RuO_2@PAN||Li/RuO_2@PAN cells at different current rates.

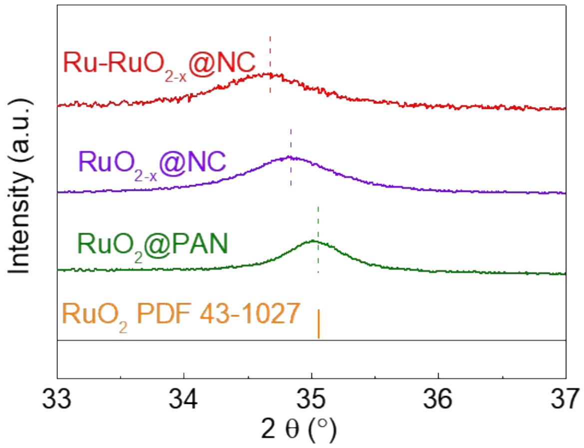

Fig. S19. Magnified XRD patterns of RuO_2@PAN, RuO_{2-x}@NC and Ru-RuO_{2-x}@NC.

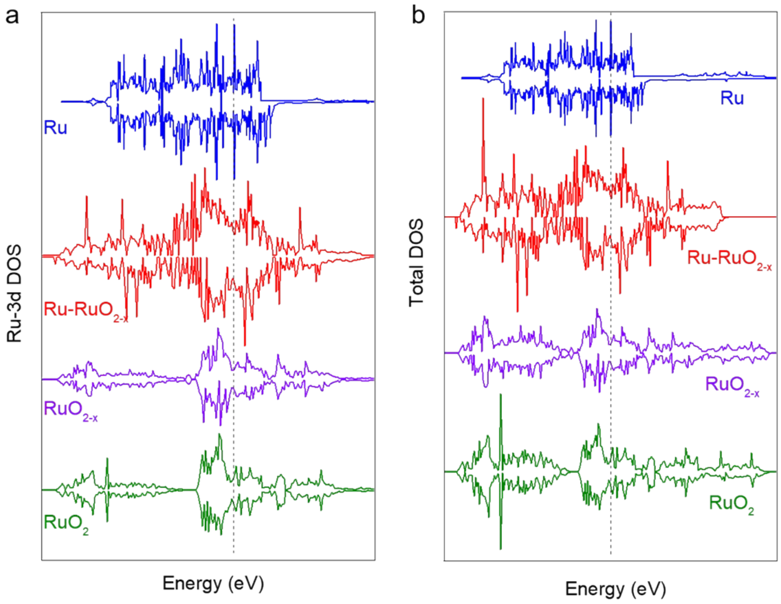

Fig. S20. (a) Ru-3d and (b) total DOS patterns of RuO_2, RuO_{2-x}, Ru-RuO_{2-x} and Ru.

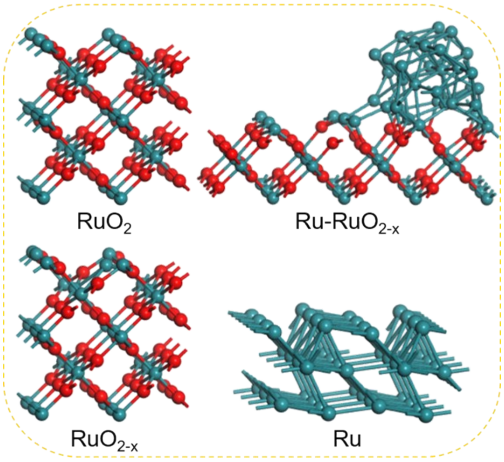

Fig. S21. Geometrically stable configurations of RuO_2, RuO_{2-x}, Ru-RuO_{2-x} and Ru.

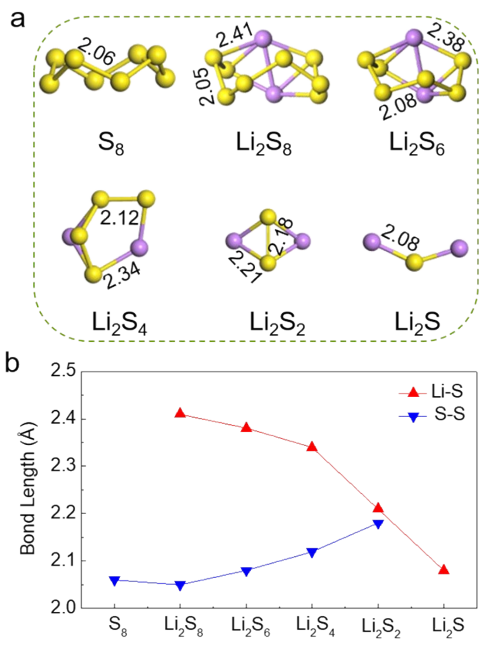

Fig. S22. (a) The optimized molecular structures of the most stable isolated LiPSs in the ground state and (b) the shortest distances of Li-S and S-S bonds.

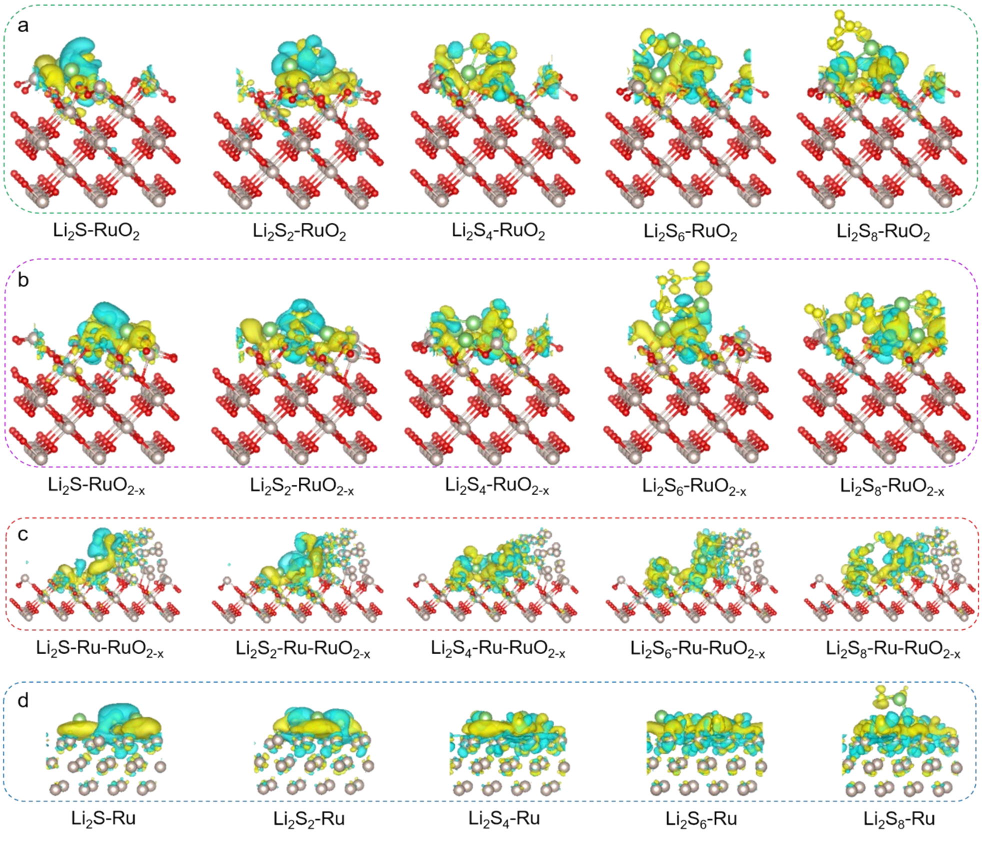

Fig. S23. DFT calculation results of optimized geometrical configurations of various LiPSs on (a) RuO_2, (b) RuO_{2-x}, (c) Ru-RuO_{2-x} and (d) Ru.

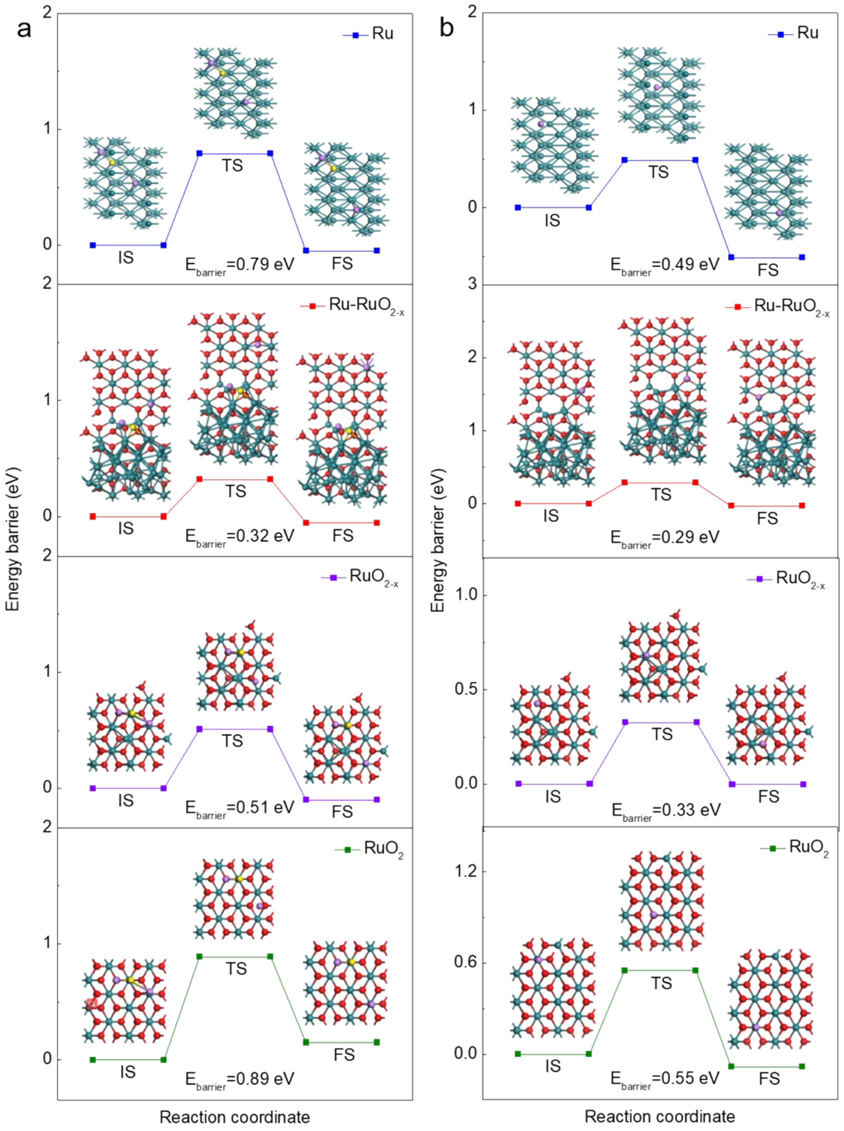

Fig. S24. (a) Energy barrier of Li_2S decomposition and (b) Li^+ diffusion energy barrier on RuO_2, RuO_{2-x}, Ru-RuO_{2-x} and Ru.

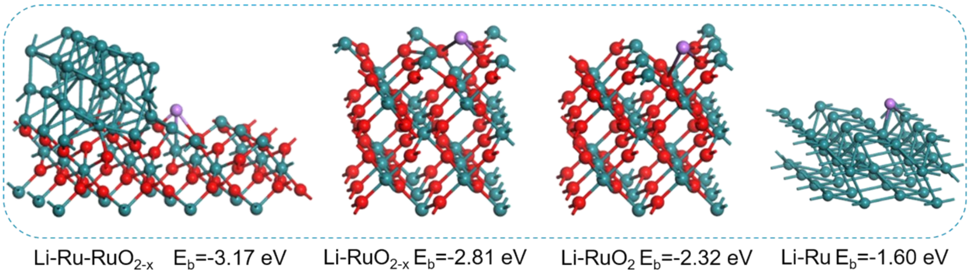

Fig. S25. Binding energy and optimized geometrical configurations of a Li atom with Ru-RuO_{2-x}, RuO_{2-x}, RuO_2 and Ru.

References

[1] R. Wang, K. Wang, S. Gao, M. Jiang, J. Han, M. Zhou, S. Cheng and K. Jiang, *Nanoscale,* 2018, **10**, 16730-16737.

[2] J. Huang, J. Q. Huang, W. G. Chong, J. Cui, S. S. Yao, B. L. Huang and J. Kim, *J. Energy Chem.,* 2019, **35***,* 204-211.

[3] Z. Y. Wang, D. D. Han, S. Liu, G. R. Li, T. Y. Yan and X. P. Gao, *Electrochim. Acta,* 2020, **337**, 135772.

[4] X. Q. Guo, H. L. Yu, X. F. Liu, Y. C. Lu, Q. C. Liu and Z. J. Li, *ChemistrySelect,* 2019, **4**, 7463-7469.

[5] Q. Lu, Y. Sun, K. M. Liao, X. H. Zou, I. Hamada, W. Zhou, M. Ni and Z. P. Shao, *Electrochim. Acta,* 2019, **298**, 421-429.